2010

Land surface brightness temperature modeling using solar insolation

Haroon Stephen
University of Nevada, Las Vegas, haroon.stephen@unlv.edu

Sajjad Ahmad
University of Nevada, Las Vegas, sajjad.ahmad@unlv.edu

Thomas C. Piechota
University of Nevada, Las Vegas, thomas.piechota@unlv.edu

Land Surface Brightness Temperature Modeling Using Solar Insolation

Haroon Stephen, Sajjad Ahmad, and Thomas C. Piechota

***Abstract*—Retrieval of land surface emissivity and temperature from microwave brightness temperature data is a complex problem. The diurnal variation of temperature due to the diurnal cycle of solar radiation and weather conditions makes this problem even more challenging. In this paper, we use solar radiation in modeling the temporal variation of the brightness temperature state of the surface. Solar insolation modeling is used to estimate the diurnal variation of land surface brightness temperature. Solar radiation and brightness temperature are linked through temperature of the surface which is derived based on the radiation balance equation. The temperature state model behaves consistent to the measured temperature data. The root-mean-square (rms) error of the model and measured temperature during 1999 is 1.47 K with a correlation of 0.98. Brightness temperature is calculated as a product of physical temperature and emissivity. This relationship is used to transform the temperature state model into the temporal model of the brightness temperature. The model is validated using Tropical Rainfall Measuring Mission (TRMM) Microwave Imager (TMI) brightness temperature observations at 10.65-GHz vertical polarization. The rms error of the modeled and measured brightness temperature during 1999 is 2.15 K with a correlation of 0.98. Physical and brightness temperature models are ordinary differential equations that are solved numerically to estimate model parameters. The model parameters are related to geophysical characteristics that modulate the temporal variation of the physical and brightness temperature. These parameters provide new insight into the thermal characteristics of the land surface. Brightness temperature model is used to retrieve emissivity from TMI measurements. Images of emissivity and other model parameters are spatially coherent and reflect ground geometrical and dielectric conditions. The results confirm that incident solar radiation is an important input in modeling the temporal variation in the physical temperature and brightness temperature.**

***Index Terms*—Brightness temperature, Colorado River basin, emissivity, microwave imager, solar insolation, Tropical Rainfall Measuring Mission (TRMM).**

I. Introduction

MICROWAVE emission is a function of thermal, dielectric, and geometrical characteristics of the surface. Spaceborne brightness temperature (T_b) measurements, which depend upon the emissivity and physical temperature, have been used to classify land surface types [1]–[6]. The emissivity of the land surface has a strong dependence on the moisture content [7]–[9] and is related to the albedo and reflectivity of the surface. Brightness temperature measurements depend upon the surface emissivity and physical temperature. Due to the complexity of natural surfaces and their thermal behavior, the retrieval of surface emissivity and temperature from the spaceborne T_b measurements is a challenging problem. Various methods have been developed to retrieve the geophysical characteristics from the T_b data. Most of these methods are based on solving the T_b model of layered media where ground, vegetation, and atmosphere are treated as different layers emitting and transmitting electromagnetic radiation [10]–[12]. These methods have been used to estimate surface albedo, canopy moisture, soil moisture, and soil reflectivity. Despite the strong forcing influence of the Sun, the diurnal variation of incident solar radiation is not incorporated in these methods. The diurnal behavior of temperature is driven by solar energy and thus incorporation of solar insolation into the T_b model can provide better insight into the thermal behavior of land.

The Tropical Rainfall Measuring Mission (TRMM) has proved to be a milestone in advancing the understanding of global rain in relation to the hydrologic cycle and climate. The TRMM Microwave Imager (TMI) is a multichannel instrument that provides dual polarization T_b measurements of the ground surface. Due to TRMM orbital geometry, TMI measurements are made at different times of day and thus the diurnal variability of surface temperature plays a major role in the temporal behavior of these measurements. The temporal variation of T_b is influenced by the surface and atmospheric conditions. The surface conditions include soil moisture, soil reflectivity, landcover, etc., whereas the atmospheric conditions primarily are cloud cover and precipitation. At longer wavelengths of TMI (e.g., 10 GHz), the contribution and attenuation by atmosphere under clear conditions is negligible. Generally, 10 GHz is considered a threshold above which the atmospheric effects become significant. Nevertheless, 10-GHz measurements are attenuated by precipitation and also indirectly influenced from cooler land surface physical temperatures under overcast conditions. Since land surface physical temperature is a function of incident solar energy, TMI 10-GHz T_b data with its diurnal sampling can be used to analyze the link between solar insolation and surface T_b response.

In this paper, we model the temporal variation of the physical and brightness temperature as a function of incident solar radiation. The approach is divided into two steps. In the first step, a temperature state model is derived from the first principles of radiation balance. In the second step, the temperature state model, along with emissivity parameter, is used to derive the temporal model of brightness temperature. The physical and brightness temperature models are in the form of ordinary

Manuscript received December 9, 2008; revised April 22, 2009 and June 5, 2009. First published September 15, 2009; current version published December 23, 2009.

The authors are with the Department of Civil and Environmental Engineering, University of Nevada, Las Vegas, NV 89154-4015 USA (e-mail: haroon.stephen@unlv.edu; sajjad.ahmad@unlv.edu; thomas.piechota@unlv.edu).

Digital Object Identifier 10.1109/TGRS.2009.2026893

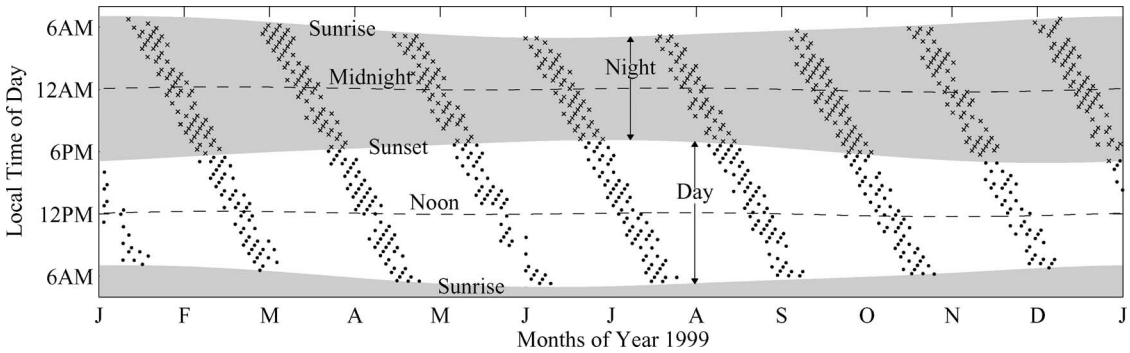

Fig. 1. Plot showing the temporal sampling of TMI T_b measurements. The time of day of the observations shifts backward as day of year progresses. The day and night times are shown by white and gray background colors, respectively, and corresponding measurements are shown as dots and crosses, respectively. The annual variation of sunrise and sunset is also shown as borders between white and gray backgrounds.

differential equations. These equations are solved numerically using the Runge–Kutta–Fehlberg method [13], [14] to compute the temporal variation of T and T_b. In order to find the model parameters that give the best model fit to the observed data, the Nelder–Mead simplex method is used to minimize the least square error between model and observed data [15]. The sensitivity of the model response to parameters is analyzed, and the models are validated using measured data. The temperature state model is validated using measured surface air temperature at a meteorological station in Walnut Gulch Experimental Watershed (WGEW) in the Lower Colorado River basin (LCRB), whereas the brightness temperature model is validated using T_b data measured by TMI. T_b model is used to estimate model parameters (emissivity) and analyze their spatial characteristics.

This paper is organized as follows. Section II describes the characteristics of the data used in this paper and the method of computing incident solar radiation. A brief description of LCRB area is also given. In Section III, the temperature state model is derived and used to determine brightness temperature model. Model simulations, as part of sensitivity analysis, are provided in Section IV. Section V presents the results and discussion. Finally, in Section VI, conclusions are presented.

II. Data

This section provides information about the data used to conduct this paper, the method used to compute incident solar radiation, and a brief description of LCRB is also given.

A. TMI

TMI is a passive multichannel instrument designed to measure rainfall. It measures the microwave energy emitted by the ground and atmosphere and is able to quantify the water vapor, cloud water, and rainfall intensity. T_b is measured at 52.75° incidence angle. TMI measures brightness temperature at five separate frequencies, i.e., 10.65, 19.35, 22.235, 37, and 85.5 GHz. Dual polarization measurements are made for each frequency except at 22.235 GHz where only vertical polarization channel is measured. The ground resolution for 10.65-GHz channel is approximately 50 km [16].

The orbit of the TRMM satellite is inclined at approximately 30°. The orbit longitude of the ascending node shifts every repeat cycle. This allows TMI to acquire T_b measurements of the target sampled at various times of day, which can be used to study diurnal response of the target. Fig. 1 shows the temporal sampling of TMI measurements during 1999. On any given day, there are only a few TMI measurements covering a particular point on the ground. TMI data collected over approximately 40-day period provides sufficiently dense time-of-day sampling of the measured brightness temperature.

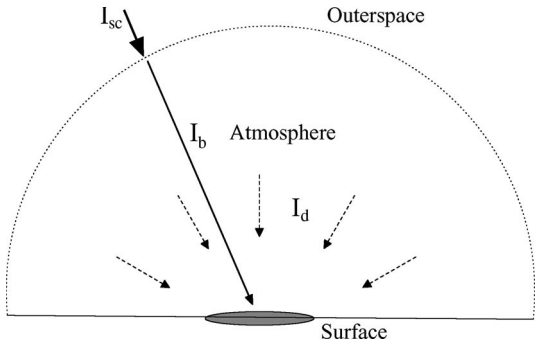

Fig. 2. Beam and diffuse components of the incident solar radiation.

B. Solar Insolation

The temporal variation of the physical temperature highly depends upon the incident solar radiation. The amount of energy that enters the Earth atmosphere is called the solar constant $(I_{\rm sc})$ and has been estimated to be an average value of 1367 W/m^2. This energy is attenuated by the atmosphere and the net energy incident on the Earth surface after attenuation is called solar insolation. Solar insolation depends upon many factors (time of day, day of year, weather, etc.). The primary reason of time-of-day and day-of-year variability lies in the Sun–Earth geometry which effects the incidence angle of the incoming radiation. Solar insolation also changes with geographical coordinates of the point of interest on the surface. The net insolation on the surface is given by

$$I = I_b + I_d \tag{1}$$

where I_b is the beam insolation and I_d is the diffuse component. The beam component is the solar energy impinging directly on the surface whereas the diffuse component is the solar energy approaching indirectly via other parts of atmosphere through

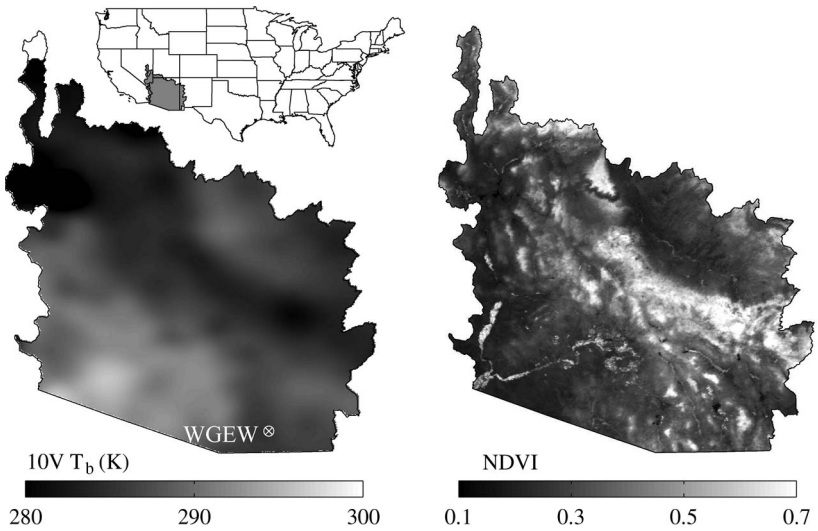

Fig. 3. (Left) Brightness temperature image of LCRB at 10.65 GHz and vertical polarization. The location of WGEW study site is also shown. (Right) Corresponding NDVI image of the area showing general vegetation landcover characteristics.

dispersion and scattering (see Fig. 2). The two components of solar insolation are given by

$$I_b = Ae^{-B\sec\theta_z}\cos\theta_z \tag{2}$$

$$I_d = CI_b \tag{3}$$

where θ_z is angle of incidence of solar energy. A, B, and C are constants that have empirically determined values. These empirical parameters vary during different times of a year and reflect the influence of the atmosphere (e.g., absorption by atmospheric species, and absorption and scattering by aerosols and clouds). The monthly average values of these parameters are adopted from the field experiment results reported by [17].

C. Colorado River Basin

Colorado River basin provides water supply and hydropower to a large area of the southwest U.S. The basin drains an area of 637 000 km^2 (246 000 mi^2), including parts of seven western U.S. states: Wyoming, Colorado, Utah, New Mexico, Nevada, Arizona, and California. It is one of the most important inner basins in the U.S. in terms of water supply for 25 million people within the basin states and adjoining areas.

Two main mountain ranges, namely, the Rocky Mountains and the Wasatch Mountains, border the east and the west of the basin. The basin contains large variations in topography, climate, soils, and vegetation. Elevations range from 1400 m to about 3700 m. The geologic parent materials provide a wide variety of soils producing vegetation from needle leaf forest complexes to mostly desert shrubs and grasses. Because of its geographic and climatologic characteristics, the Colorado River basin is particularly vulnerable to severe and sustained drought. The basin's diverse terrain characteristics are analyzed in the spatial maps of the model parameters presented in this paper. The emissivity in particular, which is linked to surface soil moisture, can help understand the ongoing drought in LCRB.

Fig. 3 shows the T_b image of LCRB at 10.65-GHz V polarization. The dark area (low T_b) in the east central LCRB is the Coconino forest along the Mogollon ridge and the brighter areas (high T_b) in the image correspond to desert and low vegetation. Corresponding normalized difference vegetation index (NDVI) image indicates similar spatial variability of vegetation cover. WGEW is located in south east region of the LCRB. Measured temperature data at this point is used for temperature state model simulation and validation.

III. Brightness Temperature Model

Brightness temperature depends upon the surface physical temperature (T) and emissivity (e) governed by the relationship

$$T_b = eT. \tag{4}$$

This relationship is an approximation of the Planck radiation law for small frequencies (Rayleigh Jean's approximation) where the brightness temperature has approximately a linear relationship with the physical temperature [7]. The physical temperature depends upon the incident energy from the Sun, and the thermal properties and thermal processes of the surface. e and T depend upon the geometrical and dielectric characteristics of the surface where the dielectric properties of the surface are linked to the moisture content and are affected by rain and evapotranspiration. Since the microwave remote sensing observations are made over an area determined by the footprint of the sensor, the observations represent the bulk characteristics within the footprint. For a given footprint surface element, the net change in the internal energy is given by

$$dE_{\text{net}} = E_{\text{in}} - E_{\text{out}} \tag{5}$$

where E_{in} and E_{out} are incoming and outgoing energies, respectively (see Fig. 4). The incoming energy includes the solar insolation (I), longwave radiation from the atmosphere, and absorption from the ground and lateral boundaries. Rees [18] has reported low contribution from downwelling radiation for frequencies below 15 GHz. The outgoing energy constitutes the emission and conduction to ground and lateral boundaries.

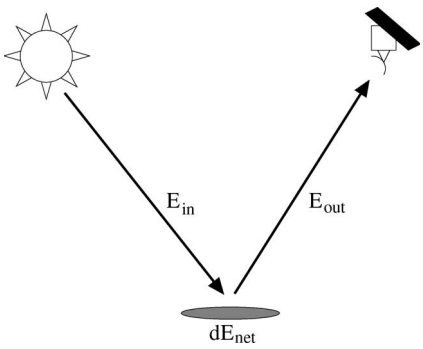

Fig. 4. Figure showing the incoming and outgoing energies used in radiation balance.

A part of the incident solar energy is absorbed by the surface and the remaining is reflected back depending upon the albedo of the surface. The absorbed energy is given by αI, where α is the broadband absorptivity of the surface. Based on Stefan–Boltzmann law, the energy emitted by the surface at temperature T is $\epsilon\sigma T^4$, where σ $(5.6704 \times 10^8$ W/m^2/K$^4)$ and ϵ denote the Stefan–Boltzmann constant and broadband emissivity, respectively. Since under thermal equilibrium $\alpha = \epsilon$, the radiation balance is given by

$$dE_{\text{net}} = \epsilon I - \epsilon\sigma T^4 + X \tag{6}$$

where X accounts for other heat and radiation exchanges with the atmosphere, subsurface, and the surrounding area. dE_{net} is related to the change in physical temperature (loss in case of cooling and gain in case of heating). This is given by

$$dE_{\text{net}} = \frac{mc}{A}\frac{dT}{dt} \tag{7}$$

where A, m, and c are the area, mass, and specific heat capacity, respectively. Letting $C_A = \epsilon A/mc$, $C_X = AX/mc$, and equating (6) and (7) results in

$$\frac{dT}{dt} = C_A[I - \sigma T^4] + C_X. \tag{8}$$

This ordinary first-order differential equation describes the state of temperature as a function of time and is forced by the solar insolation. The model relates the temperature to the solar insolation. The parameters C_A (in kelvin square meters per joule) and C_X (in kelvins per second) depend on the surface characteristics. Equations (4) and (8) together represent a state model and a measuring system, i.e.,

$$\frac{dT}{dt} = C_A[I - \sigma T^4] + C_X \text{ (State Model) and}$$
$$T_b = eT \text{ (Measuring System)}.$$

In this framework, brightness temperature measurements are samples of a continuous temperature state. The temperature state is represented by the ordinary differential equation whereas sampled measurement depends upon the state and emissivity at the time of measurement. Through this framework, T_b observations and solar insolation can be used to estimate the state and measuring system parameters.

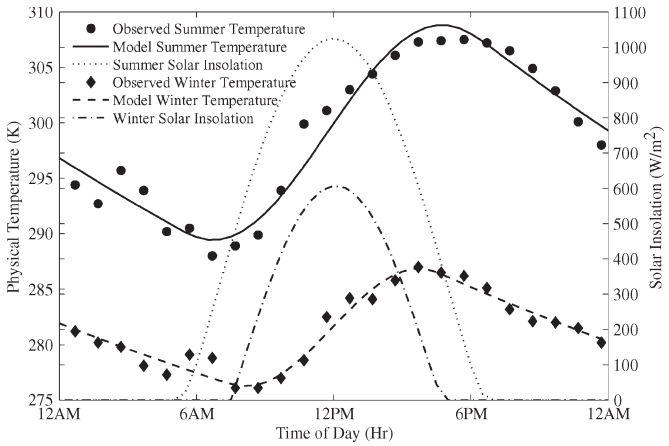

Fig. 5. Measured and modeled temperature in the WGEW during summer and winter showing the diurnal variation of temperature state and solar insolation.

Combining (4) and (8) and assuming that the emissivity of (4) does not change significantly over a short duration of time, the equations simplify to give

$$\frac{dT_b}{dt} = C_1 I - C_2\sigma T_b^4 + C_3 \tag{9}$$

where

$$C_1 = eC_A$$
$$C_2 = \frac{C_A}{e^3}$$
$$C_3 = eC_X.$$

Numerical methods are used to solve this nonlinear ordinary differential equation. The parameter e ranges between 0 and 1 and, for most natural surfaces, lies between 0.6 and 0.9 at 10 GHz. Through several test runs, it is found that C_A is a positive number with an approximate range of 0.05–0.25 and C_X ranges between 0 and 50. In order to find the model parameters, we solve the differential equation and find parameters that minimize the error between the model and observed data. Nelder–Mead minimization algorithm is used which is a multidimensional unconstrained nonlinear minimization technique [15]. The initial values of the parameters are selected within their respective acceptable ranges, and the algorithm is run to minimize the least square error between the observed and computed values. The model values are computed by solving the differential equation using the Runge–Kutta–Fehlberg method which is a popular method for solving nonstiff initial value problems [19]. This numerical solution approach is applied to (8) and (9).

IV. Model Simulation and Sensitivity Analysis

Fig. 5 shows the solution of (8) during a typical day in summer and winter. The corresponding solar insolation function is also shown. The solution is computed numerically, using the method described earlier, to fit the model to measured surface air temperature data in WGEW. Surface air temperature is measured at a 2-m height from the surface. Although the brightness temperature is more sensitive to the skin temperature, the diurnal variation is, in general, similar to the surface air

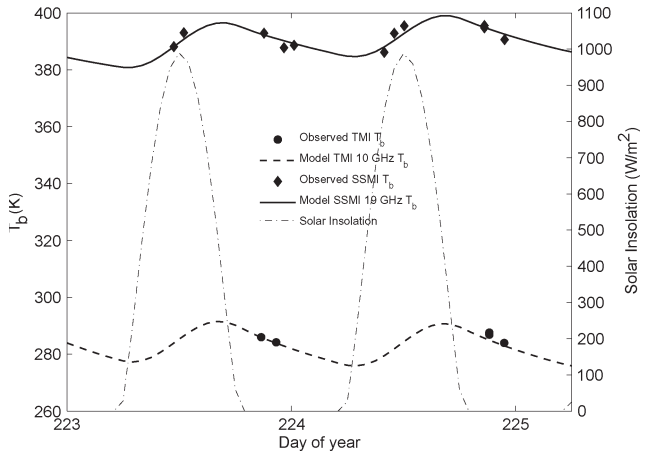

Fig. 6. Measured and modeled brightness temperature from TMI and SSMI in the WGEW showing the diurnal variation of brightness temperature and solar insolation.

temperature. The model simulation converges to a solution for most cases: If needed, repeated runs are executed by changing the initial conditions. The model converges to a solution about 90% of the time. In the 10% of the cases, the convergence is slow, and upper limit on the maximum number of iterations is exceeded. Example solutions of the run are as follows. In summer, $C_A = 0.103$ K $\cdot$ m^2/J and $C_X = 13.94$ K/s whereas in winter, $C_A = 0.116$ K $\cdot$ m^2/J and $C_X = 22.58$ K/s. The root-mean-square (rms) error for summer and winter are 1.83 and 0.81 K, respectively. The general diurnal variation of the simulated temperature is consistent with the natural temperature behavior, i.e., temperature minimum occurs around sunrise and maximum occurs after the local solar transition (noon). The model simulation represents the diurnal variation of the measured temperature quite well during summer and winter times of year.

The model is also solved for vertical polarization brightness temperature observations of TMI and special sensor microwave imager (SSMI). Data from SSMI sensors over three Defense Meteorological Satellite Program platforms, i.e., F13, F14, and F15 are combined and provide six T_b samples for a given day. Fig. 6 shows the comparison over two days of TMI 10-GHz channel and SSMI 19-GHz channel. Although the observed T_b measurements at 19 GHz are higher than 10 GHz, the diurnal variation is similar. The rms error between observed and model T_b is higher at 19 GHz (5.8 K) than at 10 GHz (3.14 K). At 19 GHz, the atmospheric effect on the T_b measurement is significant thus impacting the model performance.

In order to understand the behavior of (8), we perform simulations to analyze its sensitivity to model parameters. Given the model parameters and the temporal variation of solar insolation, (8) is solved for a given initial condition of the temperature (T_o). T_o is the temperature at zero time which is set to midnight of the first day for diurnal variation analysis. In this analysis, we run the model for five days using the solar insolation shown in Fig. 7(a). Each model parameter is changed while keeping the other parameters fixed to understand the effect on the model behavior. Fig. 7(b)–(d) shows model sensitivity to T_o, C_A, and C_X, respectively. The model is solved for five days which, through various trials, is found to be reasonable duration for the system to stabilize, provided that the chosen parameter values do not change during the time of model run. In Fig. 7(b), the model solution for three different T_o values is shown. In this figure, the diurnal variation of solar insolation does not change from day to day. No matter what the initial condition, the system reaches a steady diurnal cycle within a few days. The steady cycle is linked to the forcing function which is the amount of energy supplied to the area through solar insolation.

The parameter C_A effects the amplitude of the diurnal variation. Since it is directly proportional to the broadband emissivity, this indicates that more emissive materials go through a larger swing in their temperature during the day compared to the materials that are not very emissive [see Fig. 7(c)]. This has been observed previously in Sahel where vegetation cover removal and soil aridation reduced emissivity and thus the diurnal temperature range [20]. C_X is related to the exchange X with the surrounding atmosphere, ground and lateral boundary. The response for different values of C_X is intuitive since when more energy enters the cell from the surrounding $(C_X > 0)$, it shifts the curve to a higher diurnal mean and vice versa.

Model sensitivity analysis shows that the parameters are linked to surface characteristics that influence the amplitude and mean of diurnal cycle of physical temperature. After a few days of spin-up time, the model reaches a steady-state diurnal cycle provided that the surface conditions and diurnal solar insolation cycle do not change.

V. Results and Discussion

This section presents model parameters estimated by using the physical temperature measured in WGEW and brightness temperature measured at 10.65-GHz vertical polarization by TMI. The model is fit to the observed temperature data for each day of the year 1999. The surface conditions are assumed to change negligibly during a given day and estimated model parameters are representative of the whole day. Fig. 8(a) shows the observed and modeled temperature during selected days of 1999 at WGEW. It is evident that (8) with appropriate parameters is a good representation of the observed data. The day-to-day shift in the mean is quite well captured by the model. Fig. 8(a) shows a narrow time window of 1999 for clarity. The scatterplot in Fig. 8(b) is for all the measurements during 1999. The rms error between measured and modeled temperature is 1.47 K, and the correlation coefficient (R) is 0.98. The time series of the computed model parameters C_A and C_X [Fig. 8(c) and (d)] reveals an annual cycle which is linked to the annual variation in the surface and atmospheric characteristics. The surface characteristics effect the ϵ and X, whereas the atmospheric characteristics effect the incident solar insolation, thus indirectly influencing the optimal value of computed C_A.

Since brightness temperature measured by TMI depends upon the physical temperature, it follows a similar temporal variation. Unfortunately, on a given day, the diurnal sampling of TMI T_b data is sparse and consequently, the solution of the differential equation for optimal estimation of parameters is computed from 2–3-day T_b measurements. Fig. 9(a) shows the T_b measurements and model fit for the same period of 1999

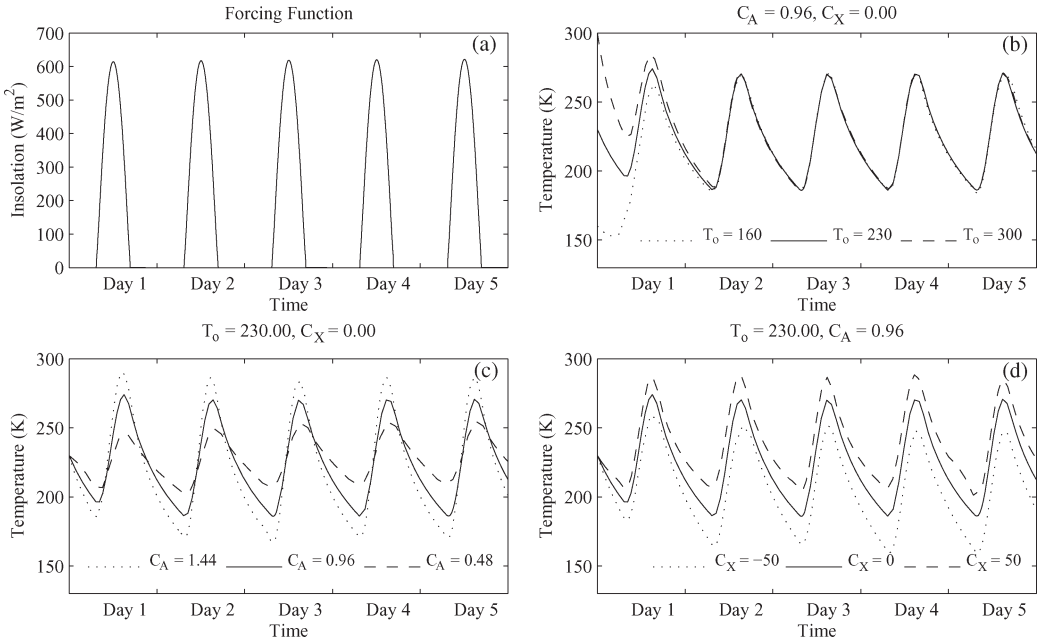

Fig. 7. Model sensitivity to various model parameters. (a) is a plot of solar insolation function used in the model simulations for a five-day period. (b)–(d) show the temperature time series from model simulations with different initial conditions. (b) is computed for three different initial temperatures. (c) and (d) plot simulations for three C_A and C_X values, respectively.

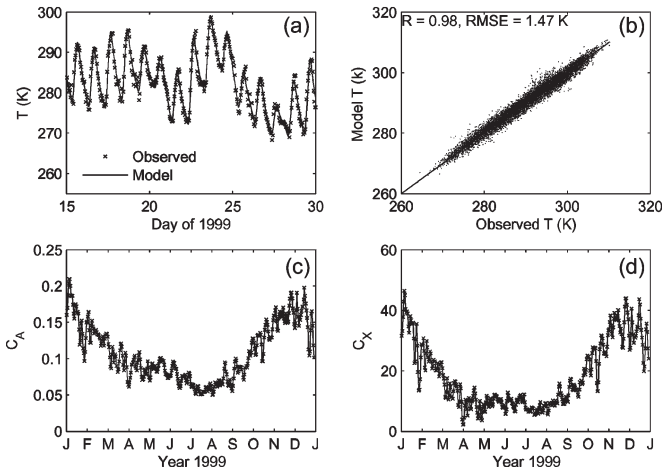

Fig. 8. (a) Model fit to measured temperature during selected days of 1999. (b) and (d) are time series plots of parameters C_A and C_X, respectively. (c) Scatter plot of measured and modeled temperature showing the rms error and correlation.

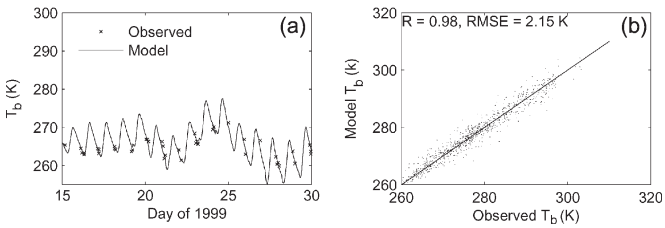

Fig. 9. (a) Model fit to TMI brightness temperature during selected days of 1999. (b) Scatter plot of measured and modeled temperature showing the rms error and correlation.

as in Fig. 8(a). For natural surfaces, T_b is less than T but, in general, follows similar temporal variation. The rms error between observed and modeled T_b is 2.15 K with a correlation coefficient of 0.98 [see Fig. 9(b)].

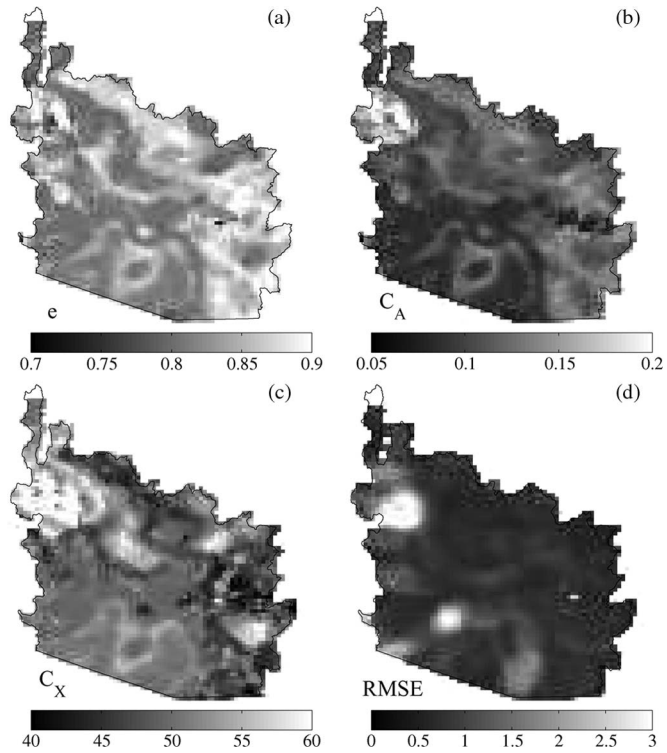

Fig. 10. Spatial maps of model parameters of (a) emissivity, (b) C_A, and (c) C_X. (d) Image of the T_b model fit rms error.

The analysis of the data in WGEW confirms the validity of the model presented. Next, the model is implemented for each grid point in the LCRB to prepare the images. TMI T_b measurements over the LCRB from Julian day 18–20 are used to estimate model parameters of (9) which are then used to compute e, C_A, and C_X. The images of these parameters are shown in Fig. 10. The spatial variation of emissivity in Fig. 10(a) reflects the spatial variation of the surface

characteristics such as vegetation type and density; soil type and density; and moisture conditions. Over the vegetated areas along the Mogollon ridge the emissivity values are high (> 0.85) whereas bare areas have relatively lower emissivities (0.8–0.85). Lake Mead has the lowest emissivities and is shown as a darker area in the Northwest part of Fig. 10(a). Fig. 10(b) and (c) shows the spatial maps of C_A and C_X, respectively, and shows the spatial coherence consistent to the features observed in the emissivity map. The surface characteristics governing these parameters are primarily the bulk thermal properties in each grid cell which depend upon the landcover, soil properties, and the water content.

The model performs well for most surface types and the highest rms error between observed and model T_b occurs over major water bodies and large urban areas. The bright spots of high error in the rms error image [Fig. 10(d)] correspond to Lake Mead and the Phoenix metropolitan area. The proposed model uses solar insolation to explain the diurnal variation of physical temperature and observed brightness temperature. Since urban areas have additional anthropogenic sources of energy contributing to the diurnal fluctuation of the temperature, the proposed model gives higher errors. The model's high error over water is probably due to the low emissivities of water: Because at low emissivities, the atmospheric noise is higher and adversely impacts the model results. Due to the large footprint of TMI 10-GHz channel, the observed measurements in the surroundings of water and urban areas, which overlap partly water or urban land, also have high rms error.

There are various sources of error that impact the performance of the proposed model. These include the atmospheric contributions and the surface inhomogeneities. Although atmospheric effects in the form of attenuation and downwelling contribution have been ignored, there impact is stronger on days with dense clouds and precipitation. Surface geometry, soil, and landcover primarily govern the thermal behavior and exchange of energy fluxes. Thus, assumption of subgrid homogeneity is also a potential source of error. Nevertheless, the results show that the proposed model can estimate the diurnal variation of the land surface physical and brightness temperature with a reasonable accuracy.

Computationally, the model is time expensive since it has to solve the differential equation at every iteration of the optimization. Nevertheless, the results provide a new insight into the relationship between solar insolation and thermal behavior of the land surface. In order to operationally implement the proposed model, other less expensive optimization techniques can be explored.

VI. Summary and Conclusion

Decoupling the effect of emissivity and surface temperature in the brightness temperature measurements is a challenging problem. The surface temperature by large depends upon the solar insolation. A simple ordinary differential equation describing the temporal variation of temperature is derived using radiation balance equation. The model is physically based and incorporates the diurnal variations of solar insolation to relate the observed temperature to the surface parameters. Earth orbital characteristics are used to compute the Sun–Earth geometry and thus estimate the solar insolation at a given point as a function of time of day and day of year.

The solution of the model depends upon the surface characteristics reflected through the model parameters. The model provides temperature time series consistent to the measured temperature data in the WGEW. A similar model of brightness temperature is also derived, and its results are consistent to the TMI observed brightness temperature measurements. The model also provides similar results with the SSMI data. The model is extended to compute the spatial maps of the model parameters that show spatially coherent features. The use of numerical methods to solve the ordinary differential equation and perform optimization makes it computationally expensive method. Nevertheless, results provide new insight into the spatial characteristics of the surface.

The developed models and analysis of simulation results show the importance of solar insolation in models of physical and brightness temperatures. These models would help in improving the retrieval of geophysical parameters from spaceborne brightness temperature measurements. Moreover, spatial maps of the bulk emissivity retrieved from the brightness temperature measurements can be related to soil moisture conditions and study the ongoing drought in the LCRB at a higher temporal resolution.

References

[1] C. Prigent, W. B. Rossow, E. Matthews, and B. Marticorena, "Microwave radiometer signatures of different surface types in deserts," *J. Geophys. Res.*, vol. 104, no. D10, pp. 12 147–12 158, 1999.

[2] K. F. Kunzi, S. Patil, and H. Rott, "Snow-cover parameters retrieved from Nimbus-7 Scanning Multichannel Microwave Radiometer (SMMR) data," *IEEE Trans. Geosci. Remote Sens.*, vol. GRS-20, no. 4, pp. 452–467, Oct. 1982.

[3] R. R. Ferrero, N. C. Grody, and J. A. Kogut, "Classification of geophysical parameters using passive microwave satellite measurements," *IEEE Trans. Geosci. Remote Sens.*, vol. GRS-24, no. 6, pp. 1008–1013, Nov. 1986.

[4] M. J. McFarland, R. L. Miller, and C. M. U. Neale, "Land-surface temperature derived from SSM/I passive microwave brightness temperatures," *IEEE Trans. Geosci. Remote Sens.*, vol. 28, no. 5, pp. 839–845, Sep. 1990.

[5] C. M. U. Neale, M. J. McFarland, and K. Chang, "Land-surface-type classification using microwave brightness temperatures from the Special Sensor Microwave/Imager," *IEEE Trans. Signal Process.*, vol. 28, no. 5, pp. 829–838, Sep. 1990.

[6] J. V. Fiore and N. C. Grody, "Classification of snow cover and precipitation using SSM/I measurements: Case studies," *Int. J. Remote Sens.*, vol. 13, no. 17, pp. 3349–3361, Nov. 1992.

[7] F. Ulaby, R. Moore, and A. Fung, *Microwave Remote Sensing: Active and Passive*, vol. 3. Norwood, MA: Artech House, 1982.

[8] T. J. Schmugge, "Remote sensing of soil moisture: Recent advances," *IEEE Trans. Geosci. Remote Sens.*, vol. GRS-21, no. 3, pp. 336–344, Jul. 1983.

[9] E. G. Njoku and D. Entekhabi, "Passive microwave remote sensing of soil moisture," *J. Hydrol.*, vol. 184, no. 1/2, pp. 101–129, Oct. 1996.

[10] E. G. Njoku and L. Li, "Retrieval of land surface parameters using passive microwave measurements at 6–18 GHz," *IEEE Trans. Geosci. Remote Sens.*, vol. 37, no. 1, pp. 79–93, Jan. 1999.

[11] E. G. Njoku, T. J. Jackson, V. Lakshmi, T. K. Chan, and S. V. Nghiem, "Soil moisture retrieval from AMSR-E," *IEEE Trans. Geosci. Remote Sens.*, vol. 41, no. 2, pp. 215–229, Feb. 2003.

[12] R. A. M. De Jeu and M. Owe, "Further validation of a new methodology for surface moisture and vegetation optical depth retrieval," *Int. J. Remote Sens.*, vol. 24, no. 22, pp. 4559–4578, Nov. 2003.

[13] M. K. Horn, "Fourth- and fifth-order, scaled Runge–Kutta algorithms for treating dense output," *SIAM J. Numer. Anal.*, vol. 20, no. 3, pp. 558–568, Jun. 1983.

[14] L. F. Shampine, "Some practical Runge–Kutta formulas," *Math. Comput.*, vol. 46, no. 173, pp. 135–150, 1986.
[15] J. A. Nelder and R. Mead, "A simplex method for function minimization," *Comput. J.*, vol. 7, no. 4, pp. 308–313, 1965.
[16] C. Kummerow, W. Barnes, T. Kozu, J. Shiue, and J. Simpson, "The Tropical Rainfall Measuring Mission (TRMM) sensor package," *J. Atmos. Ocean. Technol.*, vol. 15, no. 3, pp. 808–817, Jun. 1998.
[17] M. Iqbal, *An Introduction to Solar Radiation*. New York: Academic, 1983.
[18] G. Rees, *Physical Principles of Remote Sensing*. Cambridge, U.K.: Cambridge Univ. Press, 2001.
[19] E. Fehlberg, "Low-order classical Runge–Kutta formulas with stepsize control and their application to some heat transfer problems," George C. Marshall Space Flight Center, Huntsville, AL, Tech. Rep. NASA Tech. Rep. R-315, 1969.
[20] L. Zhou, R. E. Dickinson, Y. Tian, R. S. Vose, and Y. Dai, "Impact of vegetation removal and soil aridation on diurnal temperature range in a semiarid region: Application to the Sahel," *Proc. Nat. Acad. Sci.*, vol. 104, no. 46, pp. 17 937–17 942, 2007.

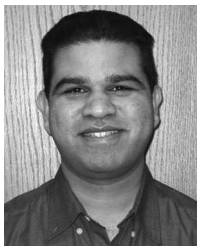

Haroon Stephen received the B.S. degree in agricultural engineering from the University of Agriculture, Faisalabad, Pakistan, in 1995, the M.S. degree in remote sensing and geographic information systems from the Asian Institute of Technology (AIT), Bangkok, Thailand, in 1997, and the Ph.D. degree in electrical and computer engineering from Brigham Young University, Provo, UT, in 2006.

During his Ph.D. studies, he conducted research at the Microwave Earth Remote Sensing Laboratory and has also instructed undergraduate classes. From 1997 to 1998, he was with the European Space Agency office, AIT, where he investigated scatterometer applications to study land surfaces. During this time, he also taught short courses in remote sensing. He is currently a Postdoctoral Researcher with the Water Resources Laboratory, Department of Civil and Environmental Engineering, University of Nevada, Las Vegas. His current research interests include microwave remote sensing applications to water resources and hydrology studies using spaceborne radars and radiometers.

Sajjad Ahmad received the B.S. degree in civil engineering from the University of Engineering and Technology, Lahore, Pakistan, in 1991, the M.S. degree in water resources from the Asian Institute of Technology, Bangkok, Thailand, in 1996, and the Ph.D. degree in civil and environmental engineering from the University of Western Ontario, London, ON, Canada, in 2002.

He is currently an Assistant Professor with the Department of Civil and Environmental Engineering, University of Nevada, Las Vegas. He is currently an Associate Editor for the *Journal of Spatial Hydrology*. His current research interests include the study of the impact of climate variability and change on water resources, stream flow forecasting using oceanic–atmospheric indices, and application of microwave remote sensing for soil moisture estimation.

Dr. Ahmad is a member of the American Geophysical Union and the American Society of Civil Engineers Committee on Emerging Technologies. He was a recipient of a National Science Foundation CAREER Grant.

Thomas C. Piechota received the B.S. degree in civil engineering from Northern Arizona University, Flagstaff, in 1989 and the M.S. and Ph.D. degrees in civil and environmental engineering from the University of California, Los Angeles, in 1993 and 1997, respectively.

He is currently the Director of Sustainability and Multidisciplinary Research and Associate Professor with the Department of Civil and Environmental Engineering, University of Nevada, Las Vegas. In his current position, he is helping move forward the Urban Sustainability Initiative which is a campus-wide effort related to sustainability-related research, education, and outreach. His teaching and research interests are in the fields of climate change, sustainability, surface water hydrology, hydroclimatology, droughts, water resources planning, and stormwater quality in urban environments. Currently, he is part of a statewide team that has received $15 000 000 in funding from National Science Foundation to study climate change in the State of Nevada.

Dr. Piechota received a National Science Foundation CAREER Award for the project "Improved Hydrologic Drought Forecasting Using Climate Information" in 2003. He is a Licensed Professional Engineer in the States of Nevada and California and serves on various committees with the American Society of Civil Engineers.